

Detached Eddy Simulation of the flow around a simplified vehicle sheltered by wind barrier in transient yaw crosswind

Marijo Telenta*, Matjaž Šubelj**, Jože Tavčar***, Jožef Duhovnik****

LECAD, Faculty of Mechanical Engineering, University of Ljubljana, Slovenia, E-mail: *marijo.telenta@lecad.fs.uni-lj.si; **matjaz.subelj@lecad.fs.uni-lj.si; ***joze.tavcar@lecad.fs.uni-lj.si; ****jozef.duhovnik@lecad.fs.uni-lj.si

 <http://dx.doi.org/10.5755/j01.mech.21.3.8942>

1. Introduction

Today's ground vehicles are sensitive to crosswind disturbance. Nonetheless, the focus of vehicle development is on providing lighter and streamlined vehicles. The vehicle's crosswind sensitivity deteriorates due to vehicle's aerodynamic design improvements. A lot of research is dedicated in analyzing the influence of the vehicle shape on the vehicle's crosswind sensitivity. There are two objectives for vehicle's aerodynamic design. The first objective is reduction of drag coefficient in order to improve fuel efficiency. The second objective is improvement of driving stability where lift and pitch are important for the straight line driving, and yawing moment and side force are important for the crosswind sensitivity [1]. However, these objectives represent conflicting goals. Therefore, in this work other means for improving crosswind sensitivity are considered. Instead of analyzing the influence of different vehicle designs on the vehicle's crosswind stability, wind barrier is considered for lowering vehicle's crosswind exposure.

Previous studies modeled fluid flow through porous geometries while not considering the details of the barrier's geometry. The main focus was to define a suitable resistance model for a given geometry of a barrier. Previous studies, [2], [3], and [4] used the Reynolds averaging method with turbulence closure for a two-dimensional fluid flow simulation in which the porous barrier was represented as a momentum sink. As stated in [5], numerical methods utilizing the momentum sink approach for wind barrier modeling treat complex unresolved flow near and through the gaps at a superficial level. A deeper understanding of the turbulent structure dynamics is required to evaluate the barrier sheltering effect. Author's previous work [6], [7] addressed this issue. URANS numerical simulations, verified with experimental data, were done modeling the fluid flow through geometrically accurate three-dimensional barrier model in order to resolve the flow near and through the porous barrier. The objective was to investigate the interaction between the bleed flow and the reverse flow for different barrier configurations. Present paper extends the research scope with more advanced turbulence models, namely Detached Eddy Simulation (DES).

DES is computationally more expensive than RANS. However, it provides more accurate results and gives information about the flow structures which is out of reach for RANS methods. RANS provides only the mean information about the flow and the unsteady information is lost. Also, flow calculation accuracy is dependent on the turbulence model used. It is difficult to define a RANS

model that accurately represents the Reynolds stresses in the region of separated flow such as a wake behind the barrier. In addition, complicated flow structures are developed in the wake region behind the barrier. These wake structures are dominated by large turbulent structures which can be resolved by DES method. Increase in the computer capability made DES simulation possible nowadays. DES is used instead of Large Eddy Simulations (LES) since LES is not feasible for higher Reynolds number flow which is the case in this work. Therefore, DES was utilized to simulate the time-development of the flow around a generic vehicle behind a wind barrier subjected to a sudden strong crosswind.

The investigation scope in the current work includes vehicle shelter by geometrically accurate wind barrier. Present numerical simulation mirrors the experimental work of [1] which is further expanded with barrier model introduction in computational domain. The goal was to analyze the barrier influence on aerodynamic loads development that vehicle is subjected to. Wind tunnel testing of a vehicle in crosswind was done in [1] where transient yaw crosswind scenario on a simplified vehicle shape corresponding to sport utility vehicle was performed. The flexibility of the CFD makes transient crosswind studies easier to realize than experimental studies. However, no DES studies with time-dependent boundary conditions investigating the wind barrier applications were found prior to this work. To date, transient crosswind with DES method has been investigated on a bus geometry [8], simple vehicle shapes [9], and high speed trains [10], [11]. In this work, unsteady crosswind simulation for sheltered moving vehicle behind the wind barrier subjected to a deterministic gust wind represented by a continuous and smooth step function is reported. Advanced boundary conditions are implemented to simulate a gust wind propagating through the computational domain. Two types of vehicle aerodynamic research are found: time-averaged aerodynamics testing and transient aerodynamic testing [12]. Time averaged technique subjects the vehicle to a constant yaw angle, whereas with the transient techniques the vehicle is subjected to a rapid change in yaw angle.

Although there are many wind induced traffic accidents every year, the wind barrier shelter effect on vehicle aerodynamic is not yet properly investigated. Available studies are still inadequate to give the complete picture of the flow structures around the moving vehicle behind the wind barrier in gust wind conditions.

2. Numerical methods

Delayed Detached Eddy Simulation (DDES) is performed to study the flow behind the wind barrier. DDES is a hybrid technique for prediction of separated turbulent flows at high Reynolds numbers. Development of this technique was motivated by the prohibitive computational costs of applying Large-Eddy Simulation (LES). Thus, high-Reynolds number separated flows have been predicted using steady or unsteady Reynolds-averaged Navier-Stokes equations (RANS and URANS). However, the disadvantage of the RANS methods applied to massive separations is that the statistical models are designed and calibrated on the basis of the mean parameters of thin turbulent shear flows containing numerous relatively standard eddies. Such eddies are not representative of the comparatively fewer and geometry-dependent structures that typically characterize massively separated flows.

Reynolds-averaged Navier-Stokes (RANS) equations, Eq. (1) and Eq. (2):

$$\frac{\partial \bar{u}_i}{\partial x_i} = 0, \quad (1)$$

$$\rho \left(\frac{\partial \bar{u}_i}{\partial t} + \bar{u}_j \frac{\partial \bar{u}_i}{\partial x_j} \right) = -\frac{\partial \bar{p}}{\partial x_i} + \mu \frac{\partial^2 \bar{u}_i}{\partial x_j \partial x_j} - \frac{\partial}{\partial x_j} \left(\overline{\rho u_j' u_i'} \right), \quad (2)$$

where \bar{p} is averaged pressure, \bar{u}_i is averaged velocity, ρ is the air density, μ dynamic viscosity, and Reynolds stresses are $\overline{\rho u_j' u_i'}$.

The filtered Navier-Stokes equations for LES, Eq. (3) and Eq. (4), are as follows [13]:

$$\frac{\partial \tilde{u}_i}{\partial x_i} = 0, \quad (3)$$

$$\frac{\partial \tilde{u}_i}{\partial t} + \frac{\partial}{\partial x_j} (\tilde{u}_i \tilde{u}_j) = -\frac{1}{\rho} \frac{\partial \tilde{p}}{\partial x_i} + \nu \frac{\partial}{\partial x_j} \left(\frac{\partial \tilde{u}_i}{\partial x_j} - \frac{\partial \tilde{u}_j}{\partial x_i} \right), \quad (4)$$

where the velocity u_i is separated into the filtered, resolved part \tilde{u}_i and sub-filtered, unresolved part u_i' , and ν is kinematic viscosity.

The switch between RANS and LES in DDES, Eq. (5) and Eq. (6), is expressed as follows [14]:

$$\tilde{d} = d - f_d \max(0, d - C_{DES} \Delta), \quad (5)$$

where:

$$f_d = 1 - \tanh\left(\left[8r_d\right]^3\right), \quad (6)$$

$$r_d = \frac{\nu_i + \nu}{\left(U_{i,j} U_{i,j}\right)^{0.5} k^2 d^2}. \quad (7)$$

Δ is the maximum edge length of the local computational cell, d distance from the wall, \tilde{d} length scale, r_d parameter, f_d function, and $C_{DES}=0.65$ is model constant.

3. Barrier and vehicle model

One barrier configuration model was used in the numerical simulation, as seen in Fig. 1, a. It consists of five horizontal bars, all with 90° inclination angle. The barrier length is $L = 9.5L_V$, where $L_V = 0.48$ m is the vehicle length. Porosity of the barrier is 25%. The computational domain is also shown in Fig. 1, b, where the barrier model length L and height H are 4.56 m and 0.4 m, respectively. Vehicle model has a box-like geometry where the width W_V and the height H_V are the same with value of 0.2 m. Ground clearance of the vehicle is 0.03 m. In order to avoid moving mesh, vehicle position is fixed and the velocity is imposed at the domain inlet.

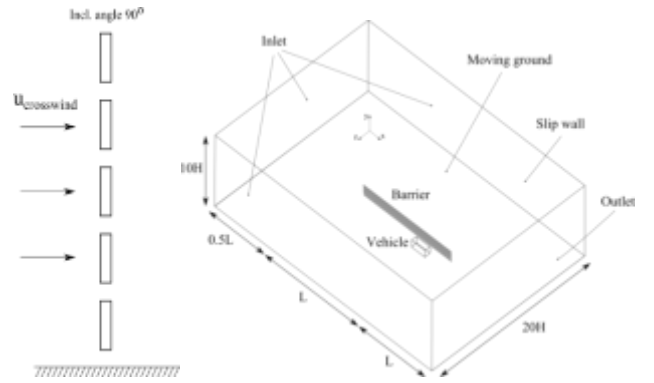


Fig. 1 (a) Barrier configuration and (b) computational domain

4. Solver

A commercial CFD code, Ansys Fluent 14.5, was used to solve incompressible Navier-Stokes equations of fluid motion. It uses cell-centered numerics, via a segregated approach, on a collocated, unstructured grid. The Delayed DES (DDES) method with the standard Spalart Allmaras (SA) model was used. The diffusive fluxes of the momentum and turbulent equations are discretized using the central difference (CD) scheme. The bounded central difference scheme was used for convective fluxes in LES and RANS regions. Second order upwind was used for the spatial discretization of the convection terms of the turbulence model. Second order upwind scheme is less diffusive and offers more accurate solution over the first order upwind scheme. The least square method was used for the gradient method. Standard pressure interpolation was used. Time integration was performed with the second-order backward Euler scheme and the bounded second-order implicit Euler scheme for turbulence variables. The DDES simulation is initialized with steady state RANS simulations. The SST $k-\omega$ turbulence model is used in RANS and simulations are run until convergence is reached. In the DDES method, pressure implicit with splitting of operator (PISO) algorithm was set for the pressure-velocity coupling. The time step is chosen to comply with the solver requirements for stability. Additionally, recommendations for time step size are followed from [15]. The time

step was set to 0.0001 s, and the CFL number for this time step was approximately 0.5.

5. Grid

The ICEM-CFD commercial grid generator software was utilized to create the numerical grid, as seen in Fig. 2. A high quality unstructured hexahedral grid was created following the recommendation for grid generation from [15]. Flow regions with different gridding requirements exist in the numerical simulation. The grid should follow the recommendations as far as possible to be efficient for the DES method. The mesh consists of O-grid and H-grid topologies. This allowed for a finer grid close to the wind tunnel walls and model surface because a no-slip boundary condition is used on those surfaces. Values of y^+ are set low (below 1) near the ground, the barrier and the vehicle surfaces. Refinement zones are created in critical areas, such as separations and wakes. Only one grid was created for the numerical simulation. However, the grid sensitivity was conducted in a prior numerical simulation where only the vehicle was analyzed under steady crosswind. Hence, a grid with 33 million elements was created, where the smallest element size was 4 mm.

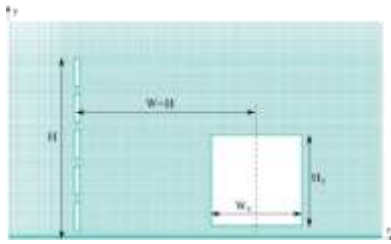


Fig. 2 Hexahedral grid with barrier and vehicle details

5.1. Assessment of the grid resolution

The resolution characteristics of the grid near the walls were discussed above by reference to the grid spacing in wall units. In the interior of the flow, the grid resolution can be assessed by comparing the grid spacing Δ to an estimate of the Kolmogorov length η .

The Kolmogorov length scale, Eq. (8), characterizes the length scale of the dissipative motion.

$$\eta = \left(\frac{\nu^3}{\varepsilon} \right)^{1/4}, \quad (8)$$

where ε is the dissipation rate and $\nu = 1.511 \times 10^{-5} \text{ m}^2/\text{s}$ is the kinematic viscosity.

Fig. 3 shows the vertical profile of the ratio Δ/η between the vehicle and the barrier, along cuts through the shear layer and in the region beyond the wall. A substantial part of the dissipation is resolved where the grid spacing is 12η . One can see from Fig. 3 that this level of discretization was achieved with levels of $\Delta/\eta < 12$ over the entire domain.

Further support for the grid resolution is provided by the ratio ν/ν_t , as seen in Fig. 4, which gives an indication of the ratio of resolved and modeled contributions to the dissipation. When eddy viscosity is larger, the RANS

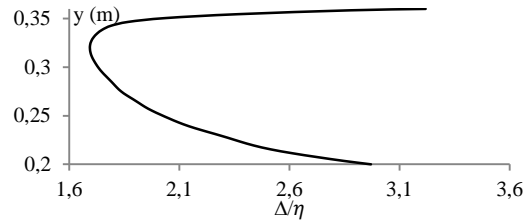


Fig. 3 Profile of the ratio Δ/η between the vehicle and the barrier

modeled contribution is larger. Higher turbulence viscosity is located near the vehicle and represents the RANS area, whereas lower turbulence viscosity represents the LES area. Fig. 4 shows the instantaneous turbulence viscosity between the vehicle and the barrier. As one can see from Fig. 4, the lower region represents the RANS region near the barrier, and the upper part represents the RANS region of the vehicle. In-between is located the LES region.

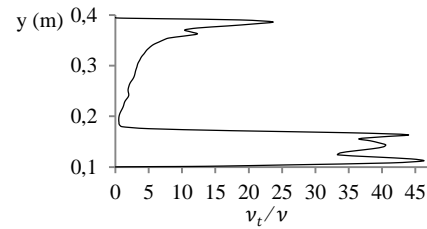


Fig. 4 Non-dimensional instantaneous turbulence viscosity

Grid dependence study was not performed. Instead, the largest feasible grid size was used, in this case hexahedral grid with 33 million elements. Since the size of the grid influences the numerical results, only one numerical simulation with largest possible grid size was performed. Instantaneous and turbulent flow is analyzed in the present work. The boundary conditions are time-dependent and therefore the data is instantaneous.

6. Boundary conditions

The dimensions of the computational domain were set to simulate open domain, as seen in Fig. 1, b. The upstream inlet and outlet were positioned at a distance of $0.5L$ upstream and L downstream from the barrier, respectively. The domain height and width were $10H$ and $20H$, respectively. No-slip boundary conditions were applied on the vehicle and the ground surfaces. Appropriate boundary layer and blockage ratio were simulated. Velocity inlet boundary condition with a uniform velocity profile was specified at the domain inlet; in this case the upstream and the lateral sides of the domain. A small turbulence intensity of 0.3% was imposed at the inlet, which corresponds to the experimental case. A pressure outlet was applied at the domain outflow. The inflow velocity was $u_v = 13 \text{ m/s}$ and maximum crosswind velocity was $u_{crosswind} = 4.73 \text{ m/s}$. The corresponding Reynolds number based on the barrier height is $Re_H = 1.7 \times 10^5$. To simulate transient gust wind, transient boundary conditions on the upstream and the lateral sides of the domain are used. In addition to the front velocity inlet, identical velocity inlet boundary conditions are specified on the lateral sides of the domain. A slip wall

boundary condition was set at the top surface of the domain. A moving wall boundary condition with 13 m/s streamwise velocity was set for the ground and the barrier surfaces, whereas a stationary wall was set for the vehicle surfaces. A moving grid was avoided with this boundary configuration. No wall functions were used for boundary layer modeling.

6.1. Unsteady crosswind

A single strong gust wind was simulated. The crosswind scenario simulates the experimental study done by [1]. A vehicle model is propelled at a constant velocity through the wind tunnel exhaust. It depicts the scenario represented in Fig. 5, a. The gust wind consists of a jet flow and two mixing layers. The jet flow was modeled as a step function where the smooth transitions represent the mixing layers, Fig. 5, b. The smooth transitions were modeled as cosine functions [9]. The maximum crosswind velocity length was set to $5L_V$, and the cosine period to $1.5L_V$. The maximum crosswind velocity was set to correspond to the 20° yaw angle of the incoming wind in respect to the vehicle. The yaw angle value of 20° is considered the most critical for vehicle safety. At the front inlet, the crosswind is only a function of time, whereas at the lateral side inlets the crosswind is a function of the time and space. The transient boundary condition was introduced in the solver via user defined functions (UDFs).

7. Results

The first 9000 time-steps are run with only headwind and were not considered because these time-steps correspond to a transient period when the flow is unsteady. This corresponds to one flow-through time, i.e., the time needed for one particle to go through the entire computational domain. Afterwards, gust wind was introduced in the computational domain.

The components of the aerodynamic forces projected on the vehicle axis are the drag in the streamwise direction, the side force in the lateral direction, and the lift in the upward vertical direction. Coherent structures of the flow are investigated by using the second invariant of the velocity gradient, the Q -criterion, Eq. (10). The visual inspection of the turbulence structures was done using the iso-surfaces of the Q -criterion.

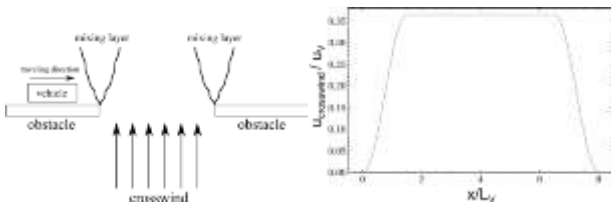


Fig. 5 (a) Crosswind scenario and (b) representative velocity profile

The definition of the Q -criterion [16]:

$$Q = C_Q (\Omega^2 - \dot{\epsilon}^2), \quad (9)$$

where $C_Q = 0.5$, $\dot{\epsilon}$ is the absolute value of the strain rate, and Ω is the absolute value of the vorticity.

$$\dot{\epsilon} = \sqrt{2\dot{\epsilon}_{ij}\dot{\epsilon}_{ij}}, \quad (10)$$

$$\Omega = \sqrt{2\Omega_{ij}\Omega_{ij}}, \quad (11)$$

$$\dot{\epsilon}_{ij} = \frac{1}{2} \left(\frac{\partial u_i}{\partial x_j} + \frac{\partial u_j}{\partial x_i} \right), \quad (12)$$

$$\Omega_{ij} = \frac{1}{2} \left(\frac{\partial u_i}{\partial x_j} - \frac{\partial u_j}{\partial x_i} \right). \quad (13)$$

7.1. Transient crosswind

The present work focuses on understanding of the flow mechanisms, which occur when the gust wind acts on the barrier and the sheltered vehicle. A time-dependent gust wind was introduced as boundary data after the headwind was first run through the computational domain. Fig. 6 shows the propagation of the gust wind through the computational domain in four different time moments: 1. no crosswind, 2. crosswind approaching the barrier, 3. crosswind approaching the vehicle, 4. crosswind behind the barrier and the vehicle.

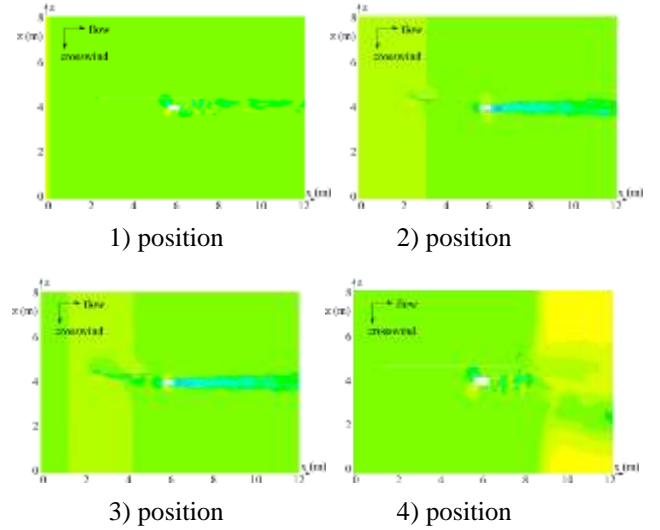


Fig. 6 Gust wind propagation colored by the velocity magnitude: 1 - no crosswind, 2 - crosswind approaching the barrier, 3 - crosswind approaching the vehicle, 4 - crosswind behind the barrier and the vehicle

7.2. Numerical accuracy

Fig. 7 shows the agreement among the characteristic points of the experimental measurements and the numerical data for no-barrier scenario. The gust length in the numerical simulation is longer for two vehicle lengths than the one from the experimental measurements, and adjustments on the time axis were performed for the experimental data to evaluate the agreement between the experimental data and the numerical results. As one can see, present results are in good agreement with the experimental measurements. In addition, Fig. 7 shows the side force coefficient trace for the fixed yaw tests. The side force coefficient value for the fixed yaw test was time-averaged. As one can see from Fig. 7, the side force coefficient for transient yaw test displays an overshoot compared

to the fix yaw test, which indicates the importance of performing the transient yaw tests for vehicle crosswind sensitivity.

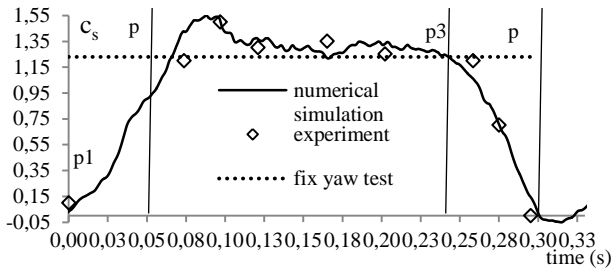


Fig. 7 The vehicle's side force coefficient without the wind barrier (p1, p2, p3, p4 are vehicle positions relative to the gust wind)

7.3. Aerodynamic forces and moments

The axis system for the force and moment coefficients is the center axis of the vehicle model, where a positive side force occurs with positive wind loading and a positive yawing moment occurs when the nose of the model turns leeward. The non-dimensional coefficients, c_F and c_M , for the forces and the moments, are defined in

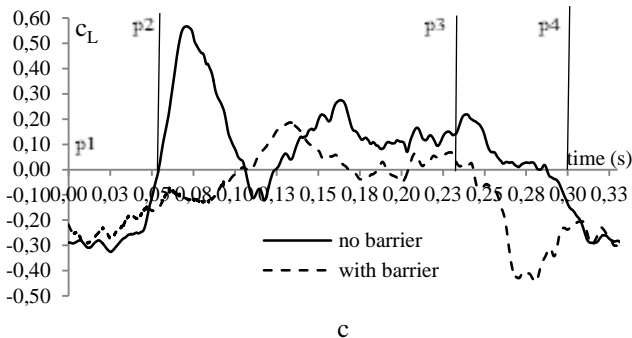
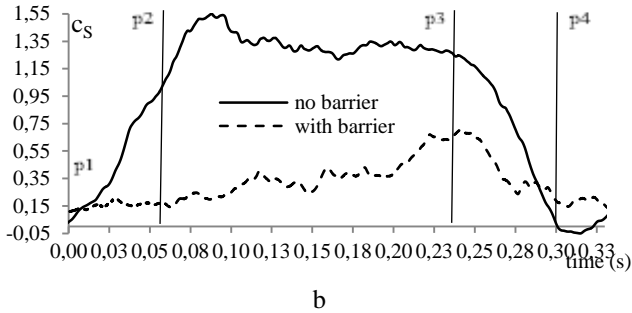
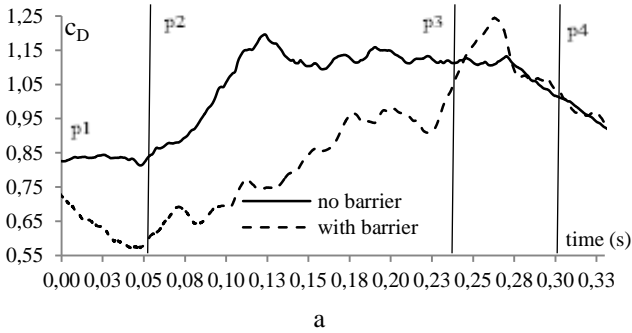


Fig. 8 Aerodynamic forces on the vehicle with and without the barrier (p1, p2, p3, p4 are vehicle positions relative to the gust wind): a - drag force coefficient, b - side force coefficient, c - lift force coefficient

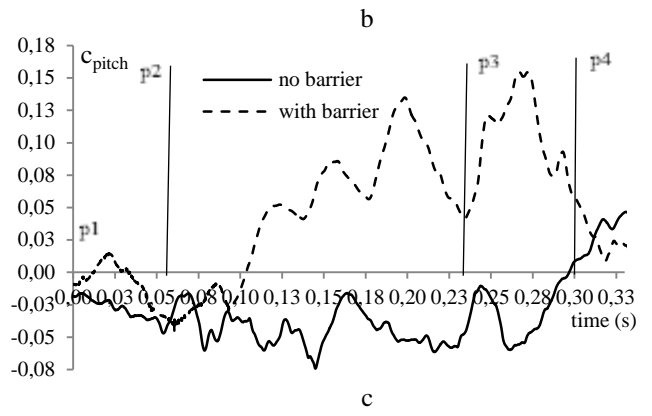
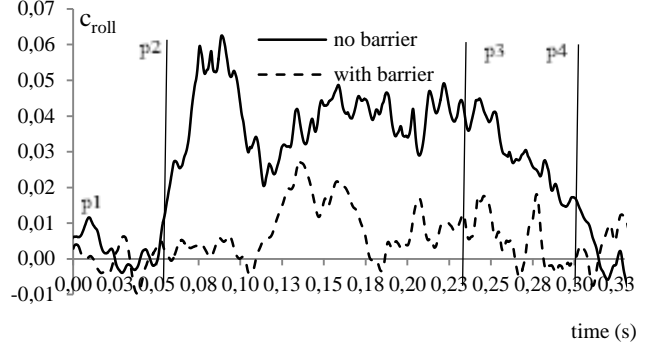
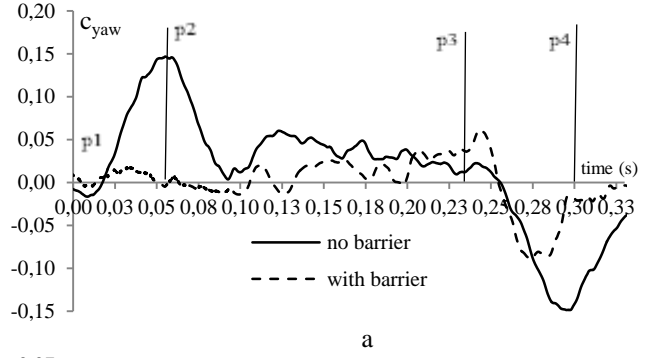


Fig. 9 Aerodynamic moments on the vehicle with and without the barrier (p1, p2, p3, p4 are vehicle positions relative to the gust wind): a - yaw moment coefficient; b - roll moment coefficient; c - pitch moment coefficient

Eq. (14) and Eq. (15):

$$c_F = \frac{F}{qA}, \tag{14}$$

$$c_M = \frac{M}{qA}, \tag{15}$$

where q is the dynamic pressure of the incoming wind, Eq. (16):

$$q = \frac{1}{2} \rho u_R^2, \tag{16}$$

where F is the force (drag, lift, and side force), M is the moment (roll, pitch, and yaw), ρ is the density of air, A is the frontal area of the vehicle model, and u_R is the resultant velocity.

The non-dimensional pressure coefficient:

$$c_p = \frac{p - p_\infty}{q}, \quad (17)$$

where p_∞ is the pressure in the free-stream.

Figs. 8-9 show the aerodynamic force and moment coefficients on the vehicle with and without the barrier, respectively. As one can see, all the aerodynamic loads are lower when the barrier is introduced except for the pitch moment coefficient. Vehicle crosswind stability is influenced mainly by the yaw moment coefficient and the side force coefficient. Hence, vehicle crosswind stability is improved significantly with the barrier shelter.

7.4. Visualization of the turbulent structures and pressure mapping

Fig. 10 shows the vehicle position relative to the gust wind. Position 1 represents the vehicle at the beginning of the gust wind. Position 2 represents the start of the vehicle experiencing the maximum velocity of the gust wind. Position 3 represents the middle of the gust wind, position 4 represents the end of the gust wind maximum velocity, at the position 5 the vehicle starts to exit the gust wind, and at the position 6 the vehicle completely exits the gust wind. Figs. 11-14 show the visual representation of the large-scale flow structures using the iso-surfaces of the Q -criterion colored by CFL value. The Q -criterion value in this work is $100\,000\text{ s}^{-2}$. One can see from Figs. 11-14 that the flow is complex and unstable. Also, the flow is

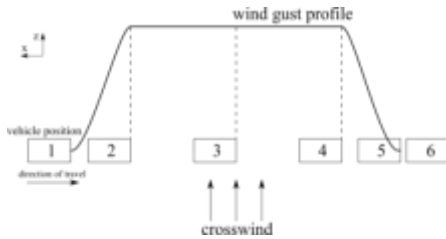


Fig. 10 Vehicle position relative to the gust wind

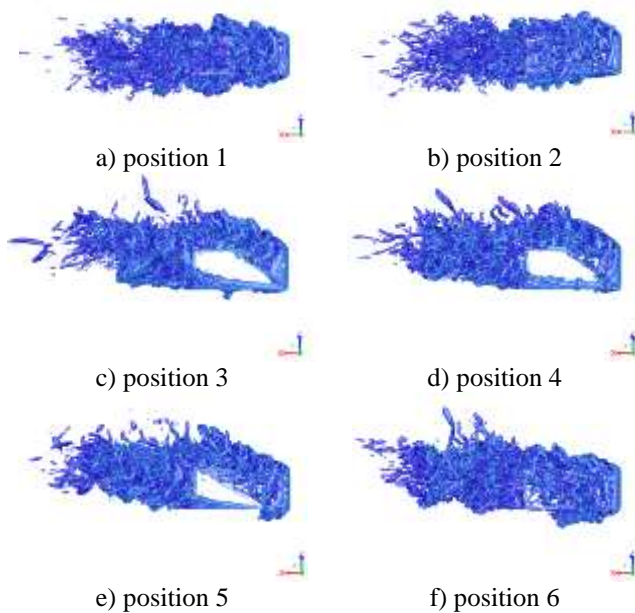


Fig. 11 Top view of the turbulence structures around the vehicle without the barrier

remarkably changed with the wind barrier introduction. There are dominant and well defined coherent vortices originating from the front surface of the vehicle at positions 3, 4 and 5 when there is no wind barrier shelter. These structures are inclined in the direction of the resultant direction of the gust wind. This is not the case for the wind barrier scenario where prevalent vortical structures are small and parallel to the vehicle traveling direction for the entire duration of the gust wind. In particular, the flow structures of the sheltered vehicle during the gust wind are similar to that before the sheltered vehicle entrance into the gust. Also, one can notice the additional vortices formed between the vehicle and the barrier.

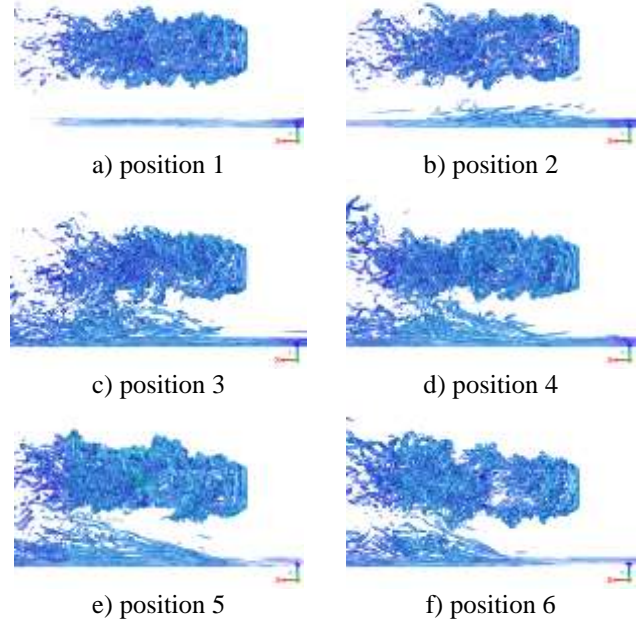


Fig. 12 Top view of the turbulence structures around the vehicle with the barrier

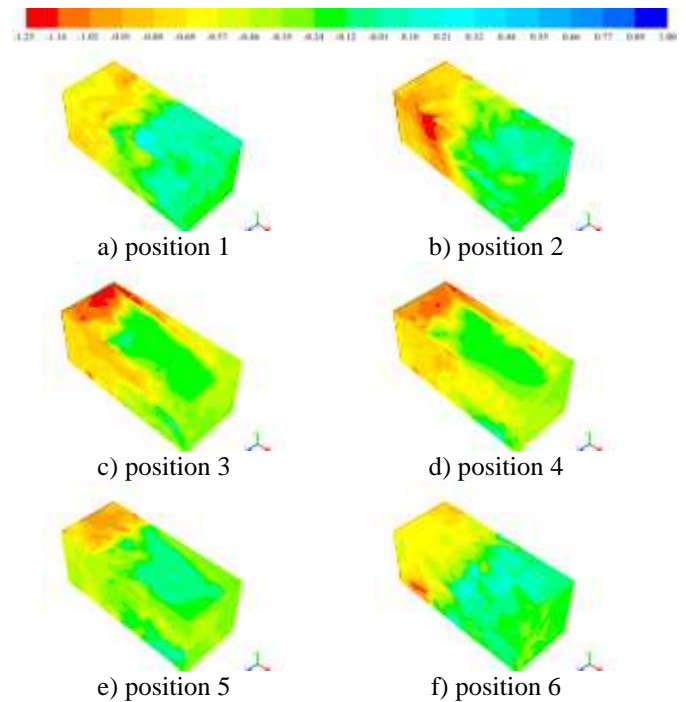


Fig. 13 Isometric view of the instantaneous pressure coefficient c_p on the vehicle without the barrier

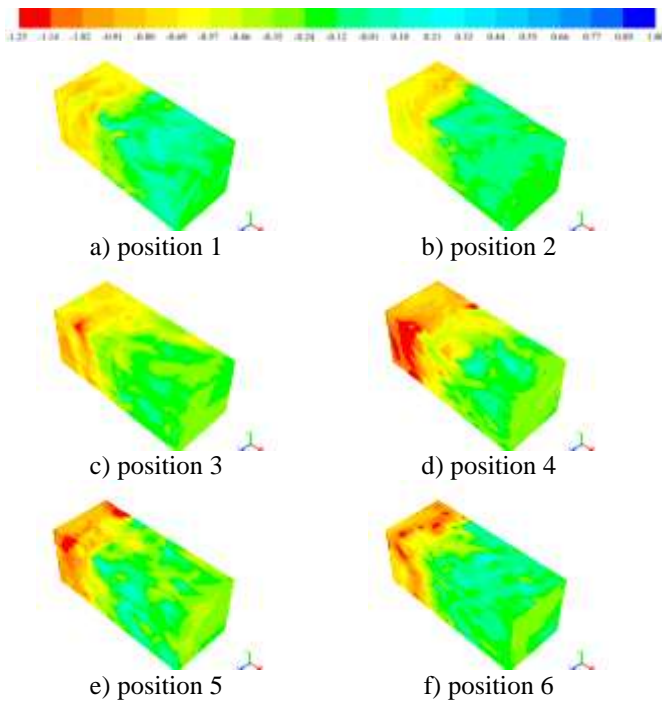


Fig. 14 Isometric view of the instantaneous pressure coefficient c_p on the vehicle with the barrier

Figs. 13-14 show the pressure distribution on the vehicle surfaces. The pressure distribution indicates the influence of the vortices on the vehicle's aerodynamic loads. As one can see, pressure coefficients are much lower for the case without the barrier shelter and consequently vehicle experiences larger aerodynamic loads. Also, one can notice in Fig. 14 that at the positions 5 and 6 higher values of the negative pressure coefficient are displayed; however, these values occur for a very short time and on a small area of the vehicle surface. In addition, one can see from Fig. 14 that at the position 4, the large negative pressure coefficient values on the vehicle's leeward surface correspond to the side force coefficient and yaw moment coefficient peak values. However, these peak values are still lower than those for the case without the wind barrier.

8. Conclusion

In this work, a geometrically accurate three-dimensional wind barrier model was used in the numerical study. An advanced aerodynamic CFD simulation, DES, was utilized in analyzing the transient crosswind scenario. Time-dependent boundary conditions were used to simulate the gust wind propagation. One barrier configuration was analyzed. Hexahedra grid with 33 million elements was used in the present numerical study. Aerodynamic coefficients, pressure mapping, and flow visualization are used to analyze the effects of the transient crosswind on the vehicle aerodynamics. The goal of this research was to quantify and visualize the barrier's shelter influence on the vehicle aerodynamics in transient crosswind scenario.

LES is not feasible for higher Reynolds number flow which is the case in this work and DES provides an accurate prediction of the dynamic change in the aerodynamic coefficient. Therefore, DES was used to investigate the influence of the barrier shelter on the vehicle aerody-

namics in gust wind. The aim was to study the flow around the vehicle in unsteady wind scenario and sheltered vehicle's aerodynamic load development. Vortical structures are significantly changed with the wind barrier application compared to the no-barrier case. Large and well defined vortical structures develop when the vehicle is not sheltered by the wind barrier. These vortical structures increase the negative pressure on the vehicle's surface which promotes increase of the vehicle aerodynamic loads. The present work shows that the vehicle aerodynamic force and moment coefficients are much lower with the barrier shelter except for the pitch moment coefficient. Moreover, vehicle's crosswind stability is improved with introduction of the wind barrier since vehicle's yaw moment coefficient and side force coefficient are significantly lower.

The present work provides insight into the vortical structure development which is result of the interaction among the vehicle, the barrier and the gust wind. It offers deeper understanding of the flow mechanism around the sheltered vehicle in the transient crosswind. In particular, the dynamics of the coherent structures, as well as the flow structure evolution and interaction with the wind barrier introduction for the vehicle protection is presented. No prior work to date has analyzed the time development of the vehicle aerodynamic loads behind the geometrically accurate wind barrier in gust wind conditions.

References

1. **Chadwick, A.** 1999. Crosswind Aerodynamics of Sport Utility Vehicle, PhD Thesis, Cranfield University.
2. **Packwood, A.** 2000. Flow through porous fences in thick boundary layers: comparisons between laboratory and numerical experiments, *J. Wind Eng. Ind. Aerodyn.* 88: 75-90.
[http://dx.doi.org/10.1016/S0167-6105\(00\)00025-8](http://dx.doi.org/10.1016/S0167-6105(00)00025-8).
3. **Fang, F.-M.; Wang, D.Y.** 1997. On the flow around a vertical porous fence, *J. Wind Eng. Ind. Aerodyn.* 67-68: 415-424.
[http://dx.doi.org/10.1016/S0167-6105\(97\)00090-1](http://dx.doi.org/10.1016/S0167-6105(97)00090-1).
4. **Huang, L.-M.; Chan, H.C.; Lee, J.-T.** 2012. A numerical study on flow around nonuniform porous fences, *J. Appl. Math.* p.12.
<http://dx.doi.org/10.1155/2012/268371>
5. **Bourdin, P.; Wilson, J.D.** 2008. Windbreak aerodynamics: Is Computational Fluid Dynamics Reliable?, *Boundary Layer Meteorol.* 126: 181-208
<http://dx.doi.org/10.1007/s10546-007-9229-y>.
6. **Telenta, M.; Duhovnik, J.; Kosel, F.; Šajin, V.** 2014. Numerical and experimental study of the flow through a geometrically accurate porous wind barrier model, *J. Wind Eng. Ind. Aerodyn.* 124: 99-108.
<http://dx.doi.org/10.1016/j.jweia.2013.11.010>.
7. **Telenta, M.** 2014 Wind barrier motorway protection. LAP LAMBERT Academic Publishing.
8. **Hassan, H.; Krajinović, S.** 2007. DES of the flow around a realistic bus model subjected to a side wind with 30 yaw angle, The fifth IASME/WSEAS International Conference on Fluid Mechanics and Aerodynamics, Athens.

9. **Favre, T.** 2011. Aerodynamics simulations of ground vehicles in unsteady crosswind, Stockholm.
<http://urn.kb.se/resolve?urn=urn:nbn:se:kth:diva-50242>.
10. **Krajnović, S.** 2008. Computer simulation of a train exiting a tunnel through a varying crosswind, *International journal of railway* 1(3): 99-105.
11. **Krajnović, S.; Ringqvist, P.; Nakade, K.; Basara, B.** 2012. Large eddy simulation of the flow around a simplified train moving through a crosswind flow, *J. Wind Eng. Ind. Aerodyn.* 110: 86-99
<http://dx.doi.org/10.1016/j.jweia.2012.07.001>.
12. **Šušteršič, G.; Prebil, I.; Ambrož, M.** 2014. The snaking stability of passenger cars with light cargo trailers, *Strojniški vestnik-Journal of Mechanical Engineering* 60: 539-548.
<http://dx.doi.org/10.5545/sv-jme.2014.1690>.
13. **Yogini P.** 2010. Numerical investigation of flow past a circular cylinder and in a staggered tube bundle using various turbulence models, *Lappeenranta*
14. **Spalart, P.; Deck, S.M.S.; Squires, K.D.** 2006. New version of detached-eddy simulation, Resistant to Ambiguous Grid Densities *Theoretical and Computational Fluid Dynamics* 20: 181-195.
<http://dx.doi.org/DOI 10.1007/s00162-006-0015-0>.
15. **Spalart, P.** 2000. Strategies for turbulence modelling and simulations, *Int. J. Heat Fluid Flow.* 21: 252-263.
[http://dx.doi.org/10.1016/S0142-727X\(00\)00007-2](http://dx.doi.org/10.1016/S0142-727X(00)00007-2).
16. **Čucitore, R.; Quadrio, M.; Baron, A.** 1999. On the effectiveness and limitations of local criteria for the identification of a vortex, *Eur. J. Mech. B/Fluids.* 18(2): 261-282.
[http://dx.doi.org/10.1016/S0997-7546\(99\)80026-0](http://dx.doi.org/10.1016/S0997-7546(99)80026-0).

Marijo Telenta, Matjaž Šubelj, Jože Tavčar,
Jožef Duhovnik

DETACHED EDDY SIMULATION OF THE FLOW AROUND A SIMPLIFIED VEHICLE SHELTERED BY WIND BARRIER IN TRANSIENT YAW CROSSWIND

S u m m a r y

This paper numerically investigates the flow around a moving vehicle sheltered by a wind barrier. Flow control strategy aimed at reducing the aerodynamic loads on the road vehicles requires a detailed knowledge of the reference flow. Exploratory study is conducted in understanding the flow physics involved in the wind barrier vehicle protection. Transient nature of the crosswind gust is represented by the time-dependent boundary conditions in Detached Eddy Simulation. Three methods to quantify and visualize the effects of the transient crosswind on the moving vehicle are considered: aerodynamic coefficients, pressure mapping, and flow visualization. Aerodynamic forces and moments acting on the vehicle are considerably lower compared to the case without the barrier shelter. Vehicle's crosswind sensitivity is improved by wind barrier application in crosswind protection. The aim of this paper is to quantify and visualize the barrier influence on the moving vehicle aerodynamics in transient crosswind scenario.

Keywords: wind barrier; vehicle aerodynamics; DES, gust wind; coherent structures.

Received December 17, 2014

Accepted March 20, 2015